# Study of $\eta$ and $\eta\prime$ Photoproduction at MAMI

V. L. Kashevarov,[1,2] P. Ott,[1] S. Prakhov,[1,3,4] P. Adlarson,[1] F. Afzal,[5] Z. Ahmed,[6] C. S. Akondi,[7] J. R. M. Annand,[8] H. J. Arends,[1] R. Beck,[5] A. Braghieri,[9] W. J. Briscoe,[3] F. Cividini,[1] R. Codling,[8] C. Collicott,[10,11] S. Costanza,[9,12] A. Denig,[1] E. J. Downie,[1,3] M. Dieterle,[13] M. I. Ferretti Bondy,[1] L. V. Fil'kov,[2] A. Fix,[14] S. Gardner,[8] S. Garni,[13] D. I. Glazier,[8,15] D. Glowa,[15] W. Gradl,[1] G. Gurevich,[16] D. J. Hamilton,[8] D. Hornidge,[17] D. Howdle,[8] G. M. Huber,[6] A. Käser,[13] S. Kay,[15] I. Keshelashvili,[13] R. Kondratiev,[16] M. Korolija,[18] B. Krusche,[13] J. Linturi,[1] V. Lisin,[16] K. Livingston,[8] I. J. D. MacGregor,[8] R. MacRae,[8] J. Mancell,[8] D. M. Manley,[7] P. P. Martel,[1,17] J. C. McGeorge,[8] E. McNicol,[8] D. G. Middleton,[1,17] R. Miskimen,[19] E. Mornacchi,[1] C. Mullen,[8] A. Mushkarenkov,[9,19] A. Neiser,[1] M. Oberle,[13] M. Ostrick,[1,*] P. B. Otte,[1] B. Oussena,[1,3] D. Paudyal,[6] P. Pedroni,[9] V. V. Polyanski,[2] A. Rajabi,[19] G. Reicherz,[20] J. Robinson,[8] G. Rosner,[8] T. Rostomyan,[13] A. Sarty,[11] D. M. Schott,[3] S. Schumann,[1] C. Sfienti,[1] V. Sokhoyan,[1,3] K. Spieker,[5] O. Steffen,[1] B. Strandberg,[8] I. I. Strakovsky,[3] Th. Strub,[13] I. Supek,[18] M. F. Taragin,[3] A. Thiel,[5] M. Thiel,[1] L. Tiator,[1] A. Thomas,[1] M. Unverzagt,[1] S. Wagner,[1] D. P. Watts,[15] D. Werthmüller,[8,13] J. Wettig,[1] L. Witthauer,[13] M. Wolfes,[1] R. L. Workman,[3] and L. Zana[15]

(A2 Collaboration at MAMI)

[1]*Institut für Kernphysik, Johannes Gutenberg-Universität Mainz, D-55099 Mainz, Germany*
[2]*Lebedev Physical Institute, 119991 Moscow, Russia*
[3]*The George Washington University, Washington, D.C. 20052-0001, USA*
[4]*University of California Los Angeles, Los Angeles, California 90095-1547, USA*
[5]*Helmholtz-Institut für Strahlen- und Kernphysik, Universität Bonn, D-53115 Bonn, Germany*
[6]*University of Regina, Regina, Saskatchewan S4S 0A2, Canada*
[7]*Kent State University, Kent, Ohio 44242-0001, USA*
[8]*SUPA School of Physics and Astronomy, University of Glasgow, Glasgow G12 8QQ, United Kingdom*
[9]*INFN Sezione di Pavia, I-27100 Pavia, Italy*
[10]*Dalhousie University, Halifax, Nova Scotia B3H 4R2, Canada*
[11]*Department of Astronomy and Physics, Saint Mary's University, Halifax, Nova Scotia B3H 3C3, Canada*
[12]*Dipartimento di Fisica, Università di Pavia, I-27100 Pavia, Italy*
[13]*Departement für Physik, Universität Basel, CH-4056 Basel, Switzerland*
[14]*Laboratory of Mathematical Physics, Tomsk Polytechnic University, 634034 Tomsk, Russia*
[15]*SUPA School of Physics, University of Edinburgh, Edinburgh EH9 3JZ, United Kingdom*
[16]*Institute for Nuclear Research, 125047 Moscow, Russia*
[17]*Mount Allison University, Sackville, New Brunswick E4L 1E6, Canada*
[18]*Rudjer Boskovic Institute, HR-10000 Zagreb, Croatia*
[19]*University of Massachusetts, Amherst, Massachusetts 01003, USA*
[20]*Institut für Experimentalphysik, Ruhr-Universität, D-44780 Bochum, Germany*

The reactions $\gamma p \rightarrow \eta p$ and $\gamma p \rightarrow \eta\prime p$ are measured from their thresholds up to the center-of-mass energy $W = 1.96$ GeV with the tagged-photon facilities at the Mainz Microtron, MAMI. Differential cross sections are obtained with unprecedented statistical accuracy, providing fine energy binning and full production-angle coverage. A strong cusp is observed in the total cross section for $\eta$ photoproduction at the energies in the vicinity of the $\eta\prime$ threshold, $W = 1896$ MeV ($E_\gamma = 1447$ MeV). Within the framework of a revised $\eta$MAID isobar model, the cusp, in connection with a steep rise of the $\eta\prime$ total cross section from its threshold, can only be explained by a strong coupling of the poorly known $N(1895)1/2^-$ state to both $\eta p$ and $\eta\prime p$. Including the new high-accuracy results in the $\eta$MAID fit to available $\eta$ and $\eta\prime$ photoproduction data allows the determination of the $N(1895)1/2^-$ properties.

DOI: [10.1103/PhysRevLett.118.212001](10.1103/PhysRevLett.118.212001)

The photoinduced production of $\eta$ and $\eta'$ mesons is a selective probe to study excitations of the nucleon. These mesons represent the isoscalar members of the fundamental pseudoscalar-meson nonet and, in contrast to the isovector $\pi$, excitations with isospin $I = 3/2$ ($\Delta$ resonances) do not decay into $\eta N$ and $\eta' N$ final states. Several single- and double-spin observables of the $\gamma p \to \eta p$ reaction have recently been measured [1–6]. A review of the experimental and phenomenological progress can be found in Ref. [7]. All model calculations [8–13] agree in the dominance of the $E_{0+}(J^P = 1/2^-)$ multipole amplitude, which is populated by the well established $N(1535)1/2^-$ and $N(1650)1/2^-$ resonances. The existence of a third $1/2^-$ nucleon resonance, however, is still under discussion. The $N(1895)1/2^-$ state is presently listed by the PDG with only two stars [14]. So far, the existing experimental data for $\eta'$ photoproduction, provided by CLAS [4,15] and CBELSA/TAPS [5], are quite scarce, especially in the near-threshold region. Recently, the threshold region attracted more attention after the first results for the beam asymmetry $\Sigma$ were presented by GRAAL [16], which, although limited in statistics, could not be reproduced by any of the existing models describing $\eta'$ photoproduction [17–21]. The threshold at $W = 1896$ MeV for the $\gamma p \to \eta' p$ reaction is located in a mass region that plays a key role for our understanding of the nucleon spectrum. Presently, there are no well established (four-star) states between $W = 1800$ and $2100$ MeV. However, there are many candidates and an even larger number of states predicted by quark models [22,23] or lattice QCD [24].

This Letter contributes to the study of $\eta$ and $\eta'$ photoproduction by presenting new high-statistics measurements of the $\gamma p \to \eta p$ and $\gamma p \to \eta' p$ differential cross sections from reaction thresholds up to $E_\gamma = 1577$ MeV ($W = 1960$ MeV). The data were obtained with a fine binning in $E_\gamma$ and cover the full range of the production angles.

The experiments were conducted by using the Crystal Ball (CB) [25] as a central calorimeter and TAPS [26] as a forward calorimeter. These detectors were installed at the energy-tagged bremsstrahlung-photon beam produced from the electron beam of the Mainz Microtron (MAMI) [27]. The beam photons were incident on a liquid hydrogen target located in the center of the CB. The energies of bremsstrahlung photons, $E_\gamma$, produced by the electrons in a $10 - \mu$m copper radiator, were analyzed by detecting postbremsstrahlung electrons in tagging spectrometers (taggers). The Glasgow-Mainz tagger [28] was used in the major part of the experiments. In order to tag the high-energy part of the bremsstrahlung spectrum, a dedicated end-point tagging spectrometer (EPT) [29] was used, especially designed for $\eta'$ measurements.

In this Letter, the analysis of three independent data sets from different periods of data taking is presented. The first data set (Run I) was taken in 2007 with the 1508-MeV electron beam and the bremsstrahlung photons analyzed by

the Glasgow-Mainz tagger up to an energy of 1402 MeV. All details on the experimental resolution of the detectors and other conditions during these measurements are given in Refs. [3,30] and the references therein. In Ref. [3], the total and differential cross sections for the $\gamma p \to \eta p$ reaction were obtained by using the $\eta \to 3\pi^0$ decay mode only. This analysis was now repeated with an improved cluster algorithm, better separating electromagnetic showers partially overlapping in the calorimeters, and with a finer angular binning, allowing a better sensitivity to higher-order partial waves. The analysis of $\eta$ photoproduction via the $\eta \to \gamma\gamma$ decay for that data set was now made for the first time. The second data set (Run II) was taken in 2009 with the 1557-MeV electron beam and the bremsstrahlung photons analyzed up to 1448 MeV. The trigger conditions for Run II required more than two clusters to be detected in the CB, which suppressed severely the detection of $\eta \to \gamma\gamma$ decays, and only $\eta \to 3\pi^0$ decays were used in the analysis of $\eta$ photoproduction. More details on the Run II conditions can be found in Ref. [31]. The third data set (Run III) was taken in 2014 with the 1604-MeV electron beam and the bremsstrahlung photons analyzed by the EPT spectrometer from 1426 up to 1576 MeV. In Run III, the threshold of $\eta'$ photoproduction was covered, and both neutral decay modes of $\eta$ and $\eta' \to \gamma\gamma$ and $\eta' \to \pi^0\pi^0\eta \to 6\gamma$ decays were analyzed. More details on the Run III conditions can be found in Ref. [29].

The selection of event candidates and the reconstruction of the outgoing particles was based on the kinematic-fit technique. Details on the kinematic-fit parametrization of the detector information and resolutions are given in Ref. [30]. The determination of the experimental acceptance for $\eta$ and $\eta'$ photoproduction and the investigation of possible background processes were based on their Monte Carlo (MC) simulations, with the generated events propagated through a GEANT simulation of the experimental setup. To reproduce the resolutions observed in the experimental data, the GEANT output was subject to additional smearing, thus allowing both the simulated and experimental data to be analyzed in the same way. For all $\eta$ and $\eta'$ decay modes used in the analysis, no background sources were found that could mimic the $\eta$ or $\eta'$ peak in the invariant-mass spectra of the corresponding decay products. However, the selection of event candidates with the kinematic fit was not sufficient to separate all background events from the actual $\eta'$ decays. Thus, the number of $\eta'$ decays observed in every energy-angle bin was obtained by fitting experimental $m(\gamma\gamma)$ and $m(\pi^0\pi^0\eta \to 6\gamma)$ spectra from the given bin with a function, describing the $\eta'$ peak above a smooth background. This procedure is illustrated for one energy-angle bin in Fig. 1, showing a typical $\eta' \to \pi^0\pi^0\eta \to 6\gamma$ invariant-mass distribution and the background shape. The uncertainty in the number of $\eta'$ decays observed is not purely statistical here, as it is based on the uncertainty in the area under the Gaussian fitted to the $\eta'$ peak. To measure the $\gamma p \to \eta' p$
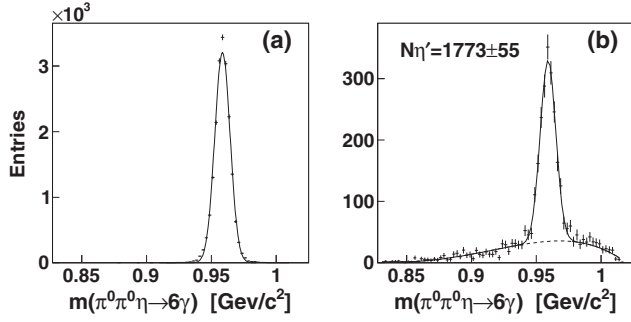
FIG. 1.   $m(\pi^0\pi^0\eta \to 6\gamma)$ distributions for $E_\gamma = 1558$ MeV and $\cos\theta = 0.1$. (a) MC simulation of $\gamma p \to \eta' p \to \pi^0\pi^0\eta p \to 6\gamma p$ with a Gaussian fit. (b) Experimental spectrum fitted with the sum of a Gaussian and a polynomial of order 4.

differential cross sections, the covered energy range, $E_\gamma = 1447$–$1577$ MeV, was divided into 12 intervals (the first four being 6.5 MeV wide and next eight 13 MeV wide), with each of them also divided into 10 $\cos\theta$ bins, where $\theta$ is the meson production angle in the center-of-mass (c.m.) frame.

To measure the $\gamma p \to \eta p$ differential cross sections, all selected events were divided into 24 $\cos\theta$ bins. For energies below $E_\gamma = 1.25$ GeV, the present analysis of the process $\gamma p \to \eta p \to 3\pi^0 p \to 6\gamma p$ was very similar to the method described in detail in Ref. [3]. At higher energies, where the remaining background could not be eliminated, the procedure for measuring $\eta \to 3\pi^0$ decays was similar to the fits described above for $\eta'$. For the process $\gamma p \to \eta p \to \gamma\gamma p$, the background could be fully eliminated below $E_\gamma = 1.15$ GeV, and the fits to the $\eta$ peak above background were needed for higher energies.

The $\gamma p \to \eta p$ and $\gamma p \to \eta' p$ differential cross sections were obtained by taking into account the number of protons in the hydrogen target, the photon-beam flux from the tagging facilities, and the $\eta$ and $\eta'$ branching ratios from Ref. [14]. For the $\eta$ cross sections, the overall systematic uncertainty resulting from the calculation of the detection efficiency and the photon-beam flux is similar to our previous analyses [2,3] and was estimated as 4% for the data taken in Run I and Run II, and as 5% for both the $\eta$ and $\eta'$ data taken in Run III. From the comparison of the differential cross section obtained from different decay modes of $\eta$ and $\eta'$, additional angular-dependent systematic uncertainties were evaluated. They included a combined effect caused by the angular resolution, the background subtraction, and the uncertainties in the angular dependence of the reconstruction efficiency. For both $\eta \to \gamma\gamma$ and $\eta \to 3\pi^0$, these kinds of additional systematic uncertainties were evaluated as 3% for the results of Run I and Run II above $E_\gamma = 1250$ MeV ($W = 1796$ MeV), and as 5% for Run III. The angular-dependent systematic uncertainty for the $\eta' \to \gamma\gamma$ results was estimated as 5%, and for $\eta' \to \pi^0\pi^0\eta \to 6\gamma$ as 6%. The latter uncertainties were added in
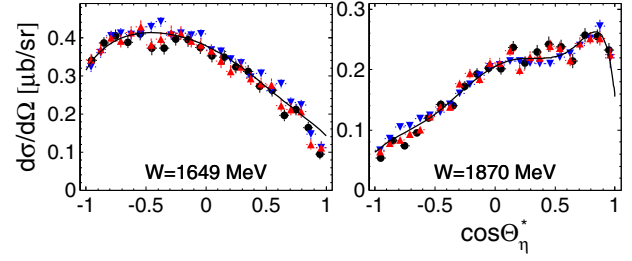


FIG. 2.   $\gamma p \to \eta p$ differential cross sections from the present analysis of Run I obtained from $\eta \to \gamma\gamma$ (the red triangles) and from $\eta \to 3\pi^0$ (the blue triangles) are shown for two energy bins and compared to the previous analysis from Ref. [3] (the black circles) based on $\eta \to 3\pi^0$ only. The error bars of all data points represent statistical uncertainties combined with the angular-dependent systematic uncertainties (which were added for $W > 1796$ MeV only). The new $\eta$MAID2017 solution is shown by the black solid line.

quadrature with the statistical uncertainties, and this sum was used to combine the results obtained from the different decay modes.

The agreement of the differential cross sections obtained for $\gamma p \to \eta p$ from different decay modes of $\eta$ is illustrated in Fig. 2 for Run I, compared also to the previous analysis of Run I [3], which was based on $\eta \to 3\pi^0$ decays only. As seen, all results are in agreement within their uncertainties. The comparison with other experiments is omitted for this energy range, as was previously demonstrated in Ref. [3]. In Fig. 3, the combined $\gamma p \to \eta p$ differential cross sections from Run I are compared to the results from Run II (based on $\eta \to 3\pi^0$ only) for two energy bins in which the largest discrepancies were observed. In Fig. 4, the combined $\gamma p \to \eta p$ differential cross sections from Run III are compared to the results from Run II, CLAS [4], and CBELSA/TAPS [5] at close energy bins. As seen, the results from Run II and Run III are consistent in the overlapping energy range. The angular dependence of both the CLAS and CBELSA/TAPS data points is very close to the present results. The results from CLAS have no full angular coverage, but they have good agreement in absolute values. The results from
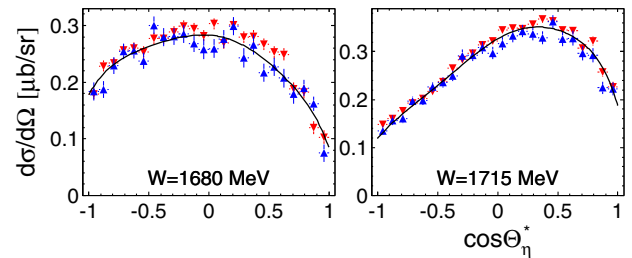


FIG. 3.   Combined $\gamma p \to \eta p$ differential cross sections from Run I (the red triangles) compared to the results from Run II (the blue triangles) for the two energy bins in which the largest discrepancies were observed. The meaning of the displayed line and error bars is the same as in Fig. 2.
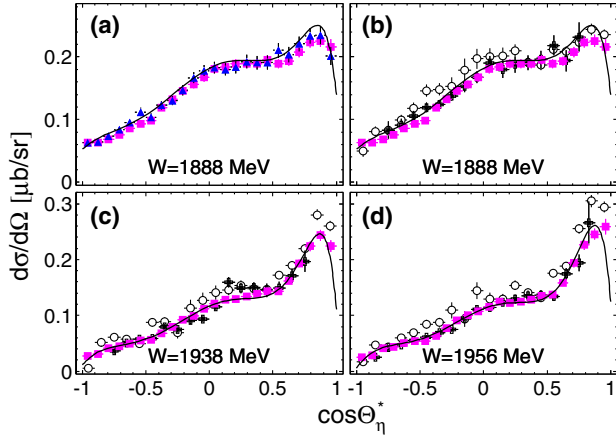
FIG. 4.  Combined $\gamma p \to \eta p$ differential cross sections from Run III (the magenta squares) compared to the results (a) from Run II (the blue triangles) and (b)–(d) from previous measurements by CLAS [4] (the black crosses) and by CBELSA/TAPS [5] (the black open circles). The meaning of the displayed line and error bars for Run II and Run III is the same as in Fig. 2. The error bars for the previous measurement represent their statistical uncertainties.



FIG. 5.  Combined $\gamma p \to \eta' p$ differential cross sections from Run III (the magenta squares) compared to the previous measurements by CLAS [4] (the black crosses) and CBELSA/TAPS [5] (the black open circles) at four overlapping energy bins. The meaning of the displayed line and error bars is the same as in Fig. 4.

CBELSA/TAPS, having full angular coverage, were obtained for much wider energy bins, and their absolute normalization is systematically higher. The latter could possibly be explained by large uncertainties of CBELSA/TAPS in the photon-flux determination (10% in Ref. [5]). In Fig. 5, the combined $\gamma p \to \eta' p$ differential cross sections from Run III are compared to the previous measurements by CLAS [4] and CBELSA/TAPS [5] at close energy bins. As seen, the uncertainties in the previous data are much larger.

The $\gamma p \to \eta p$ and $\gamma p \to \eta' p$ total cross sections, which were obtained by integrating the corresponding differential cross sections, are shown in Figs. 6 and 7 for the photoproduction of $\eta$ and $\eta'$, respectively. The comparison with previously published total cross sections illustrates much higher accuracy of the present data, especially for $\eta'$ photoproduction.

The main new feature seen in the present data for the $\gamma p \to \eta p$ total cross sections is a much more pronounced cusp at the position of the $\eta'$ threshold, marked by the vertical line in Fig. 6. Such an observation became possible due to a much finer energy binning of the present data in connection with their statistical accuracy. Compared to the previous measurement, the new $\gamma p \to \eta' p$ data span the threshold region with a much better accuracy in both the statistics and energy, allowing a much more reliable analysis of the nucleon resonances overlapping the $\eta'$ threshold region.

One of the first models dedicated to the analysis of $\eta$ and $\eta'$ photoproduction was the Mainz isobar model $\eta$MAID [13,19], which was used to fit to the data available by 2003 only. It is no surprise that those fits, shown in Figs. 6 and 7,
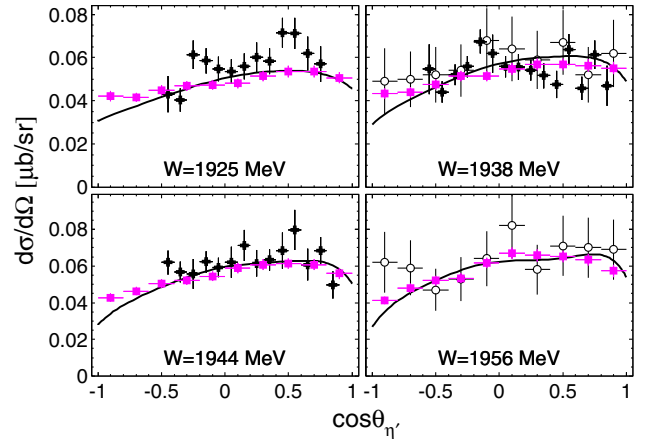
fail to reproduce more recent measurements. However, even recent analyses by SAID-GE09 [3] and BG2014-2 [8] are also far from agreement with the new $\eta$ data, and there were no solutions of those models for the $\eta'$ data. A model analysis of the previous $\eta'$ data is illustrated by the calculations from Ref. [35].

For a better interpretation of the new $\eta$ and $\eta'$ data, a new $\eta$MAID2017 model has been developed, based on the ideas
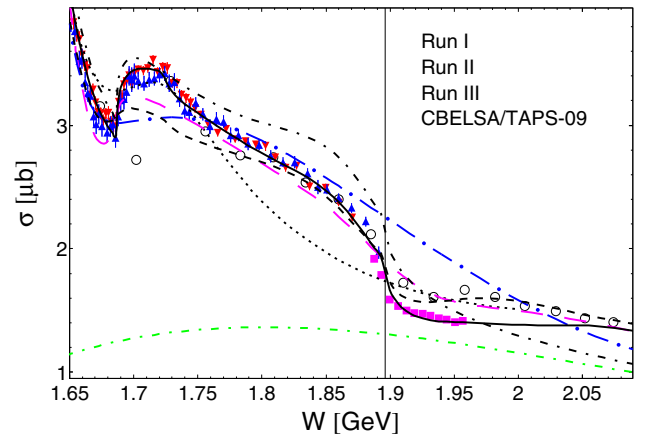


FIG. 6.  $\gamma p \to \eta p$ total cross sections from this Letter compared to the previous measurements by CBELSA/TAPS [5] and to model calculations by $\eta$MAID-2003 [13] (the black dotted line), SAID-GE09 [3] (the blue long-dashed-dotted line), BG2014-2 [8] (the magenta long-dashed line). The notation for the new $\eta$MAID2017 solution and the meaning of the error bars are the same as in Fig. 4. The Regge background and its sum with the contributions from $N1/2^-$ resonances are shown by green and black dashed-dotted lines, respectively. The $\eta$MAID2017 solution from the fit only to the previous $\eta$ and $\eta'$ data is shown by the black dashed line. The vertical line corresponds to the $\eta'$ threshold.
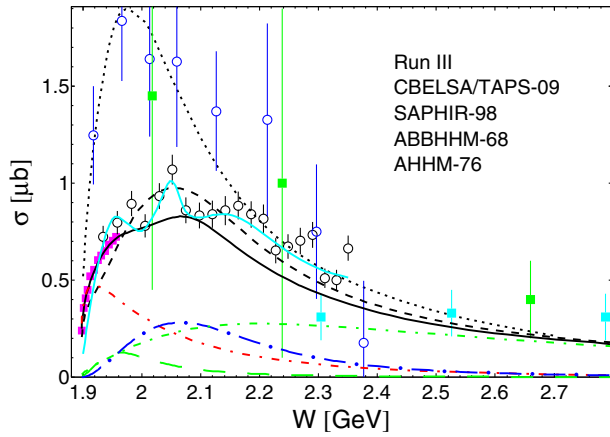
FIG. 7. $\gamma p \to \eta' p$ total cross sections from this Letter compared to the previous measurements by CBELSA/TAPS [5], SAPHIR [32], ABBHHM [33], and AHHM [34], and to the model calculations by the $\eta$MAID-Regge-2003 [19] and $\eta$MAID2017 solutions (with the same notations as in Fig. 6 and statistical uncertainties shown for the previous measurements). The fit to the CBELSA/TAPS data from Ref. [35] is shown by the cyan solid line. For the final $\eta$MAID2017 solution, the individual contributions from $N(1895)1/2^-$, $N(1900)3/2^+$, and $N(2120)3/2^-$ are shown by the red dashed-dotted, green long-dashed, and blue long-dashed-dotted lines, respectively.

of $\eta$MAID [13,19]. The new model includes a nonresonant background, which consists of the vector ($\rho$ and $\omega$) and axial-vector ($b_1$) exchange in the $t$ channel, and $s$-channel resonant excitations. Regge trajectories for the meson exchange in the $t$ channel were used to provide correct asymptotic behavior at high energies. In addition to the Regge trajectories, Regge cuts with natural and unnatural parities were included according to the ideas developed in Ref. [36] for pion photoproduction. Nucleon resonances in the $s$ channel were parametrized with Breit-Wigner shapes. The major role for the description of $\eta$ and $\eta'$ photo-production is played by the three $s$-wave resonances: $N(1535)1/2^-$, $N(1650)1/2^-$, and $N(1895)1/2^-$, the last of which plays a key role in the features observed at the $\eta'$ threshold. Both the exact shape of the cusp in the $\eta$ photoproduction and the steepness of $\eta'$ photoproduction at threshold are strongly correlated with the properties of $N(1895)1/2^-$ (having only a two-star status [14]), allowing their extraction with good accuracy. The impact of the new data from this Letter on constraining the $N(1895)1/2^-$ properties is illustrated by comparing two fits of the $\eta$MAID2017 model to the data available for $\eta$ and $\eta'$ photoproduction on protons [1,2,4–6,16], which were made before and after including the new data. As seen in Figs. 6 and 7, the fit only to the previous data fails to describe either the cusp in the new $\eta$ cross sections or the rise of the $\eta'$ cross sections from its threshold, leaving large uncertainties in the parameters determined for $N(1895)1/2^-$. Including the new high-accuracy data in the fit provides, in addition to a much better description of the entire spectrum, a much stronger

TABLE I. Fit results for $J^P = 1/2^-$ resonances. Breit-Wigner parameters: mass $M_{BW}$, width $\Gamma_{BW}$, branching ratio to $\eta N$ channel $\beta_{\eta N} = \Gamma_{\eta N}(M_{BW})/\Gamma_{BW}$, and helicity amplitude $A_{1/2}$ in units of $10^{-3}$ GeV$^{-1/2}$, which was fixed during the fit. The stars in the first column indicate the overall status of the resonance. The first row for each resonance gives a parameter set of the new $\eta$MAID solution. The second row lists the corresponding parameters from PDG [14], the averaged values of which are not given there for $N(1895)1/2^-$.

| Resonance $J^P$ | $M_{BW}$ [MeV] | $\Gamma_{BW}$ [MeV] | $\beta_{\eta N}$ [%] | $A_{1/2}$ |
|---|---|---|---|---|
| $N(1535)1/2^-$ | $1528 \pm 6$ | $163 \pm 25$ | $41 \pm 4$ | $+115$ |
| **** | $1535 \pm 10$ | $150 \pm 25$ | $42 \pm 10$ | $+115 \pm 15$ |
| $N(1650)1/2^-$ | $1634 \pm 5$ | $128 \pm 16$ | $28 \pm 11$ | $+45$ |
| **** | $1655^{+15}_{-10}$ | $140 \pm 30$ | $14\text{–}22$ | $+45 \pm 10$ |
| $N(1895)1/2^-$ | $1890^{+9}_{-23}$ | $150 \pm 57$ | $20 \pm 6$ | $-30$ |
| ** | | | | |

constraining for the $N(1895)1/2^-$ properties. The parameters determined for all three $s$-wave resonances are presented in Table I. The comparison of the fit results for the two four-star states with their known parameters [14] confirms the quality of the new data and the reliability of $\eta$MAID2017 model. As the mass obtained for $N(1895)1/2^-$ is below the $\eta'N$ threshold, the effective branching ratio of $\beta_{\eta'N} = (38 \pm 20)\%$ was calculated by integrating the decay spectrum above the $\eta'N$ threshold according to Ref. [37]. The contribution of $N(1895)1/2^-$ to the $\gamma p \to \eta' p$ total cross section is compared in Fig. 7 to the contributions of the other two resonances, $N(1900)3/2^+$ and $N(2120)3/2^-$, important in this energy range.

In summary, photoproduction reactions $\gamma p \to \eta p$ and $\gamma p \to \eta' p$ are measured from their thresholds up to the c.m. energy $W = 1.96$ GeV with the A2 tagged-photon facilities at MAMI. Differential cross sections are obtained with unprecedented statistical accuracy, providing fine energy binning and full production-angle coverage. A strong cusp is observed in the total cross section for $\eta$ photoproduction at the energies in the vicinity of the $\eta'$ threshold, $W = 1896$ MeV ($E_\gamma = 1447$ MeV). Within the revised $\eta$MAID isobar model, this cusp, in connection with the steep rise of the $\eta'$ total cross section from its threshold, can only be explained by a strong coupling of $N(1895)1/2^-$ to both channels. Including the new high-accuracy data in the analysis by the revised $\eta$MAID allows the determination of the poorly known properties of $N(1895)1/2^-$ with better precision.

---

*ostrick@kph.uni-mainz.de

[1] I. Senderovich et al., Phys. Lett. B **755**, 64 (2016).
[2] J. Akondi et al., Phys. Rev. Lett. **113**, 102001 (2014).
[3] E. F. McNicoll et al., Phys. Rev. C **82**, 035208 (2010).
[4] M. Williams et al., Phys. Rev. C **80**, 045213 (2009).
[5] V. Crede et al., Phys. Rev. C **80**, 055202 (2009).
[6] O. Bartalini et al., Eur. Phys. J. A **33**, 169 (2007).
[7] V. Krusche and C. Wilkin, Prog. Part. Nucl. Phys. **80**, 43 (2015).
[8] A. V. Anisovich, E. Klempt, V. A. Nikonov, A. V. Sarantsev, and U. Thoma, Eur. Phys. J. A **47**, 153 (2011); A. V. Anisovich, R. Beck, E. Klempt, V. A. Nikonov, A. V. Sarantsev, and U. Thoma, Eur. Phys. J. A **48**, 15 (2012).
[9] R. L. Workman, M. W. Paris, W. J. Briscoe, and I. I. Strakovsky, Phys. Rev. C **86**, 015202 (2012).
[10] V. Shklyar, H. Lenske, and U. Mosel, Phys. Rev. C **87**, 015201 (2013).
[11] H. Kamano, S. X. Nakamura, T.-S. H. Lee, and T. Sato, Phys. Rev. C **88**, 035209 (2013).
[12] D. Rönchen, M. Döring, H. Haberzettl, J. Haidenbauer, U.-G. Meißner, and K. Nakayama, Eur. Phys. J. A **51**, 70 (2015).
[13] W.-T. Chiang, S. N. Yang, L. Tiator, and D. Drechsel, Nucl. Phys. A**700**, 429 (2002).

[14] C. Patrignani et al. (Particle Data Group), Chin. Phys. C **40**, 100001 (2016).
[15] M. Dugger et al., Phys. Rev. Lett. **96**, 062001 (2006).
[16] P. Levi Sandri et al., Eur. Phys. J. A **51**, 77 (2015).
[17] K. Nakayama and H. Haberzettl, Phys. Rev. C **73**, 045211 (2006).
[18] F. Huang, H. Haberzettl, and K. Nakayama, Phys. Rev. C **87**, 054004 (2013).
[19] W.-T. Chiang, S. N. Yang, L. Tiator, M. Vanderhaeghen, and D. Drechsel, Phys. Rev. C **68**, 045202 (2003).
[20] X.-H. Zhong and Q. Zhao, Phys. Rev. C **84**, 065204 (2011).
[21] V. A. Tryasuchev, Phys. Part. Nucl. Lett. **10**, 315 (2013).
[22] S. Capstick and W. Roberts, Prog. Part. Nucl. Phys. **45**, S241 (2000).
[23] M. Ronniger and B. C. Metsch, Eur. Phys. J. A **47**, 162 (2011).
[24] R. G. Edwards, N. Mathur, D. G. Richards, and S. J. Wallace, Phys. Rev. D **87**, 054506 (2013).
[25] A. Starostin et al., Phys. Rev. C **64**, 055205 (2001).
[26] R. Novotny, IEEE Trans. Nucl. Sci. **38**, 379 (1991); A. R. Gabler et al., Nucl. Instrum. Methods Phys. Res., Sect. A **346**, 168 (1994).
[27] K.-H. Kaiser et al., Nucl. Instrum. Methods Phys. Res., Sect. A **593**, 159 (2008).
[28] J. C. McGeorge et al., Eur. Phys. J. A **37**, 129 (2008).
[29] P. Adlarson et al., Phys. Rev. C **92**, 024617 (2015).
[30] S. Prakhov et al., Phys. Rev. C **79**, 035204 (2009).
[31] P. Aguar-Bartolomé et al., Phys. Rev. C **88**, 044601 (2013).
[32] R. Plotzke et al., Phys. Lett. B **444**, 555 (1998).
[33] ABBHHM Collaboration, Phys. Rev. **175**, 1669 (1968).
[34] W. Struczinski et al., Nucl. Phys. B**108**, 45 (1976).
[35] F. Huang, H. Haberzettl, and K. Nakayama, Phys. Rev. C **87**, 054004 (2013).
[36] A. Donnachie and Yu. S. Kalashnikova, Phys. Rev. C **93**, 025203 (2016).
[37] J. Beringer et al. (Particle Data Group), Phys. Rev. D **86**, 010001 (2012).